

Detection of Flare-associated CME Candidates on Two M-dwarfs by GWAC and Fast, Time-resolved Spectroscopic Follow-ups

J. WANG,^{1,2} L. P. XIN,² H. L. LI,² G. W. LI,² S. S. SUN,^{1,2,3} C. GAO,^{1,2,3} X. H. HAN,² Z. G. DAI,⁴ E. W. LIANG,¹
X. Y. WANG,⁴ AND J. Y. WEI^{2,3}

¹*Guangxi Key Laboratory for Relativistic Astrophysics, School of Physical Science and Technology, Guangxi University, Nanning 530004, Peoples Republic of China*

²*Key Laboratory of Space Astronomy and Technology, National Astronomical Observatories, Chinese Academy of Sciences, Beijing 100101, Peoples Republic of China*

³*School of Astronomy and Space Science, University of Chinese Academy of Sciences, Beijing, Peoples Republic of China*

⁴*School of Astronomy and Space Science, Nanjing University, Nanjing, 210000, Peoples Republic of China*

ABSTRACT

The flare-associated stellar coronal mass ejection (CME) in solar-like and late type stars is quite essential for the habitability of an exoplanet. In this paper, we report detection of flare-associated CMEs in two M-dwarfs, thanks to the high cadence survey carried out by the Ground Wide-angle Camera system and the fast photometric and spectroscopic follow-ups. The flare energy in R -band is determined to be 1.6×10^{35} erg and 8.1×10^{33} erg based on the modeling of their light curves. The time-resolved spectroscopic observations start at about 20 and 40 minutes after the trigger in both cases. The large projected maximum velocity of $\sim 500 - 700$ km s⁻¹ suggests that the high velocity wing of their H α emission lines are most likely resulted from a CME event in both stars, after excluding the possibility of chromospheric evaporation and coronal rain. The masses of the CMEs are estimated to be $1.5 - 4.5 \times 10^{19}$ g and 7.1×10^{18} g.

Keywords: stars: flare — stars: late-type — stars: coronae

1. INTRODUCTION

Highly energetic flares with a total energy of 10^{33-39} erg have been frequently reported for solar-like and late-type main-sequence stars in multi wavelength (e.g., Pettersen 1989; Schmitt 1994; Osten et al. 2004; 2005; Huenemoerder et al. 2010; Balona 2015; Notsu et al. 2016; Van Doorselaere et al. 2017; Kowalski et al. 2013; Davenport et al. 2016; Chang et al. 2018; Paudel et al. 2018; Schmidt et al. 2019; Xin et al. 2021). It is now commonly accepted that the flares are resulted from the stellar magnetic activity, such as magnetic reconnection (e.g., Noyes et al. 1984; Wright et al. 2011; Shulyak et al. 2017). In the flares, the heated chromospheric plasma moves upward and is confined in the erupted magnetic field line, which leads to an expectation of a large-scale expulsion of the confined plasma, i.e., coronal mass ejection (CME), triggered by magnetic reconnection, if the field eruption is strong enough and

the overlying fields are not too constraining (see a review in Forbes et al. 2006). The energy released in reconnection heats the plasma and eject it into interplanetary space (e.g., Tsuneta 1996; Kliem et al. 2000; Karlicky & Barta 2007; Li et al. 2016).

The linkage between flares and CMEs has been, in fact, firmly demonstrated in the Sun. Solar observations indicate that the CME occurrence, mass, and energy increase with the flare energy¹ (e.g., Yashiro et al. 2008; Aarnio et al. 2011; Webb & Howard 2012). However, the CMEs detected on other active stars with stronger magnetic fields and more energetic flares are still rare at the current stage (e.g., Moschou et al. 2019). The detection and study of stellar CMEs are essential for evaluating the habitability of an exoplanet, because gas-dynamic simulation suggests that the frequent stellar CMEs can tear off most of the atmosphere of an exoplanet (e.g., Cherenkov et al. 2017).

Corresponding author: J. Wang, H. L. Li
wj@nao.cas.cn, lhl@nao.cas.cn

¹ The relationship is in fact roughly valid for stellar CMEs, when their flare X-ray luminosity is involved (Moschou et al. 2019).

Due to a lack of enough spatial resolution, detection of stellar CMEs is still a hard task for current instruments. Even though, two methods based on Doppler-shift and X-ray (and EUV) absorption have been developed to detect stellar CMEs. We refer the readers to Moschou et al. (2019) for a brief review. Based on the large blue wing of $H\gamma$ emission line, Houdebine et al. (1990) reported the fastest CME with a projected maximum velocity of 5800 km s^{-1} on M-dwarf AD Lec. Koller et al. (2021, and references therein) recently identified six CME candidates with an excess at the Balmer line wing by a systematic search in the archival SDSS spectral database. A more definite evidence of stellar CMEs can be learned from Argiroffi et al. (2019), who detected a delayed and blueshifted ($-90 \pm 30 \text{ km s}^{-1}$) $O \text{ VIII} \lambda 18.97 \text{ \AA}$ emission line on active star HR 9024 by time-resolved high-resolution X-ray spectroscopy taken by the Chandra X-ray Observatory space telescope. Moschou et al. (2017) reported a temporal decay of the X-ray absorption in the superflare on the eclipsing binary Algol, which can be interpreted by an absorption by an expanding CME. A claim of stellar CME based on the EUV dimming (e.g., Chandra et al. 2016) can be found in Ambruster et al. (1989).

In this paper, we report a claim of detection of CMEs in the flares of two M-dwarfs triggered by the GWAC system. The fast and time-resolved spectroscopy enables us to investigate the temporal evolution of the Balmer emission-line profiles, and to identify the flare-associated CMEs according to their high-velocity line wings. The paper is organized as follows. Section 2 describes the discovery of the two flares. The photometry and spectroscopic follow-ups, along with the corresponding data reductions, are outlined in Sections 3 and 4, respectively. Section 5 presents the light curve and spectral analysis. The results and discussion is shown in Section 6.

2. DETECTION OF FLARES BY GWAC

Ground-based Wide-Angle Cameras (GWAC) system, which aims to detect fast optical transients by a high cadence down to 15 seconds, is one of the ground facilities of SVOM mission². The whole system contains a set of cameras each with a diameter of 18cm and a Field-of-View of 150 deg^2 , and a set of follow-up telescopes. With the cadence, the limiting magnitude of the cameras is down to $R \sim 16.0 \text{ mag}$. The follow-up observations in image can be carried out by the dedicated two 60 cm telescopes (GWAC-F60A/B) and one 30 cm tele-

scope (GWAC-F30), which are all deployed beside the cameras. Now, the GWAC system is located at Xinglong observatory, National Astronomical Observatories of Chinese Academy of Sciences (NAOC). We refer the readers to Wang et al. (2020) and Xin et al. (2021) for the more detailed description of the GWAC system.

Table 1 tabulates the log of the two flares, i.e., GWAC 201221A and GWAC 211117A, discovered by the GWAC system. The typical localization error determined from the GWAC images is about $2''$ in both cases. Figure 1 shows the discovery images and the corresponding reference images taken by the GWAC cameras. In both cases, the shapes of the image profile of the two transients are very similar to the point spread function (PSF) of the nearby bright objects, suggesting a high probability that they are not hot pixels. The two transients did not show any apparent motion among the several consecutive images. There are also no known minor planets or comets³ brighter than $V = 20.0 \text{ mag}$ within a radius of $15'$. Also, no known variable stars or CVs can be found in SIMBAD around the transient positions within $1'$.

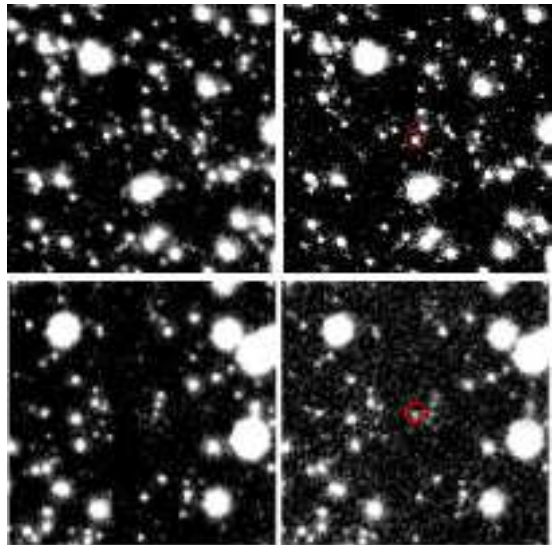


Figure 1. Discovery of GWAC 201221A (the two upper panels) and GWAC 210117A (the two lower panels) by the GWAC system. In each row, the left and right panels show the reference image and discovery image, respectively. The size of all images is $19.5' \times 19.5'$. The transients are marked by the red circles in the discovery images.

For each of the cases, an off-line pipeline involving a standard aperture photometry was performed at the location of the transient and for several nearby bright

² SVOM is a ChinaFrance satellite mission dedicated to detect and study Gamma-ray bursts (GRBs). Please see the White Paper given in Wei et al. (2016) for the details.

³ <https://minorplanetcenter.net/cgi-bin/mpcheck.cgi?>

reference stars by using the IRAF⁴ APPHOT package, including the corrections of bias, dark and flat-field and a differential photometry in a standard manner. The actual brightness of each transient was then obtained by a calibration by using the SDSS catalogues through the Lupton (2005) transformation⁵. The calculated discovery brightness, along with the quiescent brightness, in R -band are shown in Column (5) in Table 1. The corresponding specific flux in R -band at the

quiescent state is $f_R = 8.8 \times 10^{-17} \text{ erg s}^{-1} \text{ cm}^{-2} \text{ \AA}^{-1}$ and $1.4 \times 10^{-16} \text{ erg s}^{-1} \text{ cm}^{-2} \text{ \AA}^{-1}$ for GWAC 201221A and GWAC 210117A, respectively. The distance listed in the Column (10) is obtained by an inverse of the parallax provided in the Gaia catalog. With the distance, the total luminosity in R -band at the quiescent state is estimated to be $L_R = 1.5 \times 10^{30} \text{ erg s}^{-1}$ and $9.4 \times 10^{29} \text{ erg s}^{-1}$ for GWAC 201221A and GWAC 210117A, respectively.

⁴ IRAF is distributed by the National Optical Astronomical Observatories, which are operated by the Association of Universities for Research in Astronomy, Inc., under cooperative agreement with the National Science Foundation.

⁵ <http://www.sdss.org/dr6/algorithms/sdssUBVRITransform.html/#Lupton2005>

Table 1. Two Optical Transients Discovered by the GWAC System.

Transient ID	Trigger time	R.A.	Decl	Discovery/quiescent mag	Quiescent counterpart	Gaia DR2 ID	<i>G</i> -band	GBp-GRp	<i>d</i>
	(UT)	(J2000)	(J2000)	(mag)			(mag)	(mag)	(pc)
(1)	(2)	(3)	(4)	(5)	(6)	(7)	(8)	(9)	(10)
GWAC 201221A	17:50:36	07:39:08.8	+17:14:32	13.7/18.25	SDSS J073908.7+171435.3	3169102436090768768	17.557 ± 0.002	3.01	295.5 ± 15.8
GWAC 210117A	16:06:33	08:39:42.0	+20:17:45	14.5/17.75	EPIC 212002525	664439416447387392	17.081 ± 0.002	2.98	188.9 ± 4.8

NOTE—Column (1): the ID of the confirmed transient triggered by the GWAC system. Column (2): the discovery time in UT. Columns (3) and (4): the celestial coordinate at J2000 equinox. Column (5): discovery brightness in *R*-band. Columns (6) and (7): the name of the quiescent counterpart and the corresponding source ID in the Gaia DR2 catalog. Column (8): the quiescent brightness in *G*-band extracted from the Gaia DR2 catalog. Column (9): the Gaia GBp-GRp color index of the quiescent counterpart. Column (10): the distance in parsec that is obtained by an inverse of the observed parallax.

3. PHOTOMETRIC FOLLOW-UPS AND DATA REDUCTION

Each transient was followed-up in photometry immediately by the GWAC-F60A telescope in the standard Johnson-Cousins R -band. The dedicated real-time automatic transient validation system (RAVS, Xu et al. 2020) enables us to identify the transient in minutes and to carry out a monitor with an adaptive sampling. The sampling is optimized basing upon the brightness and the evolution trend of individual target.

The properties of the quiescent counterparts of the two transients are tabulated in Table 1 as well. Column (7), (8) and (9), respectively, list the G -band brightness, GBP-GRp color and distance of the quiescent counterparts, extracted from the Gaia DR2 catalog (Gaia Collaboration et al. 2018a).

Raw images taken by the GWAC-F60A telescope were reduced again by following the standard routine in the IRAF package, including bias and flat-field corrections. The standard aperture photometry and calibration based on the SDSS catalogues through the Lupton (2005) transformation were adopted for building the light curves. The final light curves are shown in Figure 2 for the two flares. Note that the effect of reddening can be safely ignored in both cases throughout the current study, because the extinctions in the Galactic plane along the line-of-sight are as low as $E(B - V) = 0.03\text{mag}$ and $E(B - V) = 0.05\text{mag}$ for GWAC 201221A and GWAC 210117A, respectively, based on the updated dust reddening map provided by Schlafly & Finkbeiner (2011).

4. SPECTROSCOPY AND DATA REDUCTION

After the discovery and identification of the two flares, time-resolved long-slit spectroscopy was performed by the NAOC 2.16m telescope (Fan et al. 2016) as soon as possible through the Target-of-Opportunity mode. The log of the spectroscopies are shown in Table 2, where Δt is the time delay between the start of the first exposure of spectroscopy and the trigger time. In total, we have 11 and 7 spectra for GWAC 201221A and GWAC 210117A, respectively. The epochs of the start and end of the spectroscopy are marked by the arrows in Figure 2.

All the spectra were taken by the Beijing Faint Object Spectrograph and Camera (BFOSC) that is equipped with a back-illuminated E2V55-30 AIMO CCD. The grating G8 with a wavelength coverage of 58008200Å was used in the observations since we focus on $H\alpha$ emission line. With a slit width of $1.8''$ oriented in the south-north direction, the spectral resolution is 3.5 Å as measured from the sky lines, which corresponds to a velocity

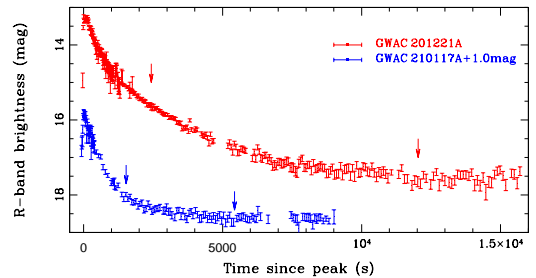


Figure 2. R -band light curves of GWAC 201221A (red symbols) and GWAC 210117A (blue symbols) observed by GWAC and F60A. The peak times correspond to MJD=59205.243714 day and MJD=59232.170581 day for GWAC 201221A and GWAC 210117A, respectively. For each flare, the arrows mark the start and end of our time-resolved spectroscopy.

of 160 km s^{-1} at the $H\alpha$ emission lines. The wavelength calibrations were carried out with the ironargon comparison lamps, and the flux calibrations with the observations of the Kitt Peak National Observatory standard stars (Massey et al. 1988). The airmass ranges from 1.1 to 1.3 during the observations.

We reduced the two-dimensional spectra by the standard procedures, including bias subtraction and the flat-field correction, by using the IRAF package again. For each of the transients, fixed apertures of both object and sky emission were used in the spectral extraction for both object and corresponding standard, which is essential for building the differential spectra (see Section 4 for the details). All of the extracted one dimensional spectra were then calibrated in wavelength and in flux by the corresponding comparison lamp and standards. The accuracy of the wavelength calibration is 0.1Å for both flares as assessed by the sky emission lines. The extracted spectra are shown in Figure 3. At first glance, a significant descend with time can be learned from both $H\alpha$ and He I λ 6678 emission lines.

5. LIGHT CURVE AND SPECTRAL ANALYSIS

5.1. Light curve analysis

In order to estimate the total energy released in the flares, the light curves are analyzed by following Xin et al. (2021) who modeled the decay phase of a $\Delta R \sim 9.5$ mag flare of a ultra-cool main sequence star more or less

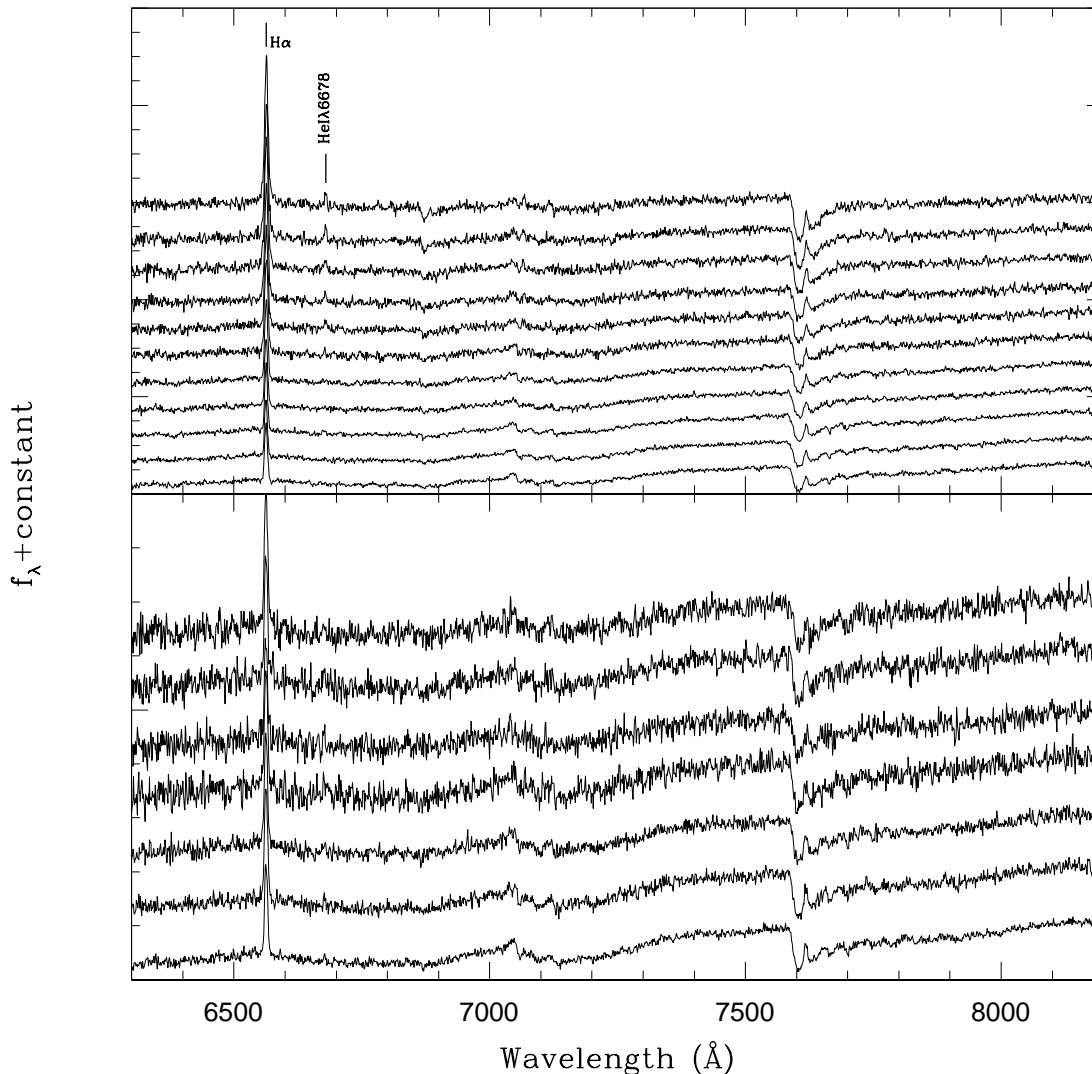


Figure 3. The time-resolved spectroscopies of GWAC 201221A and GWAC 210117A are displayed in the upper and lower panels, respectively. In each panel, the spectra are sorted with time from top to bottom, and shifted vertically by an arbitrary amount for visibility. The H α and He I λ 6678 emission lines are marked on the top panel.

by the method described in Davenport et al. (2014). We at first calculate F_{amp} , the peak relative flux normalized to the quiescent level in R -band (see Section 2) from the peak brightness, after transforming the GWAC magnitudes to the R -band through the method described early in Section 2. Taking into account of the GWAC’s high cadence of 15 second, the detected peak magnitude is simply adopted as the real peak brightness of the flare. F_{amp} is resulted to be 100 and 20 for GWAC 201221A and GWAC 210117A, respectively.

With the determined F_{amp} , we then model each light curve by two separate phases.

- **Rising phase.** By following Xin et al. (2021), we model the rising phase by a linear relationship for the cases with rare detection:

$$\frac{F_{\text{rise}}}{F_{\text{amp}}} = a_0 + k_0 t \quad (1)$$

where F_{rise} is the relative flux normalized to the quiescent level.

- **Decaying phase.** After the peak brightness, both light curves can be modeled by a template being composed of a sum of three exponential components, the template proposed in Davenport et al. (2014). The template used in the current study is

Table 2. Log of Spectroscopic Observations Carried Out by the NAOC 2.16m Telescope.

ID	Sp. Number	Exposure time (s)	S/N of H α
(1)	(2)	(3)	(4)
GWAC 201221A		$\Delta t = 40.55\text{min}$	
	1	600	56.1
	2	600	48.5
	3	600	55.9
	4	600	43.4
	5	600	35.1
	6	600	39.5
	7	1200	45.6
	8	1200	39.8
	9	1800	31.6
	10	1800	27.1
	11	1800	31.1
GWAC 210117A		$\Delta t = 25.55\text{min}$	
	1	300	20.0
	2	300	16.4
	3	300	11.3
	4	600	14.4
	5	600	20.1
	6	600	24.4
	7	1200	34.2

NOTE—Column (1): the ID of the confirmed transient triggered by the GWAC system. Column (2): the number series of spectrum. Column (3): the exposure time in unit of second. Column (4): the measured signal-to-noise ratio of the H α emission line (see section 5.2 for the details).

a sum of three exponential components, standing for the impulsive decay phase, the gradual decay phase and the late shallow decaying phase:

$$\frac{F_{\text{decay}}}{F_{\text{amp}}} = \sum_{i=1}^3 k_i e^{-a_i \frac{t}{t_{1/2}}} \quad (2)$$

where $t_{1/2} = 1$, a parameter describing the full time width at half the maximum flux, is adopted in our modeling (Xin et al. 2021).

The best modelings of the light curves of the two flares are shown in Figure 4. The best-fit parameters, along with the reduced χ^2 , are tabulated in Table 3. In GWAC 210117A, a few of measurements with an evident deviation are excluded in the modeling. We argue that the corresponding small value of the reduced χ^2 is likely due to the large photometric uncertainty at the end of the decaying. With the modeling, the equivalent duration (ED) of a flare, defined as the time needed to emit all the flare energy at a quiescent flux level (e.g., Kowalski et al. 2013), is therefore determined to be 11223 and 8820 seconds for GWAC 201221A and GWAC 210117A, respectively.

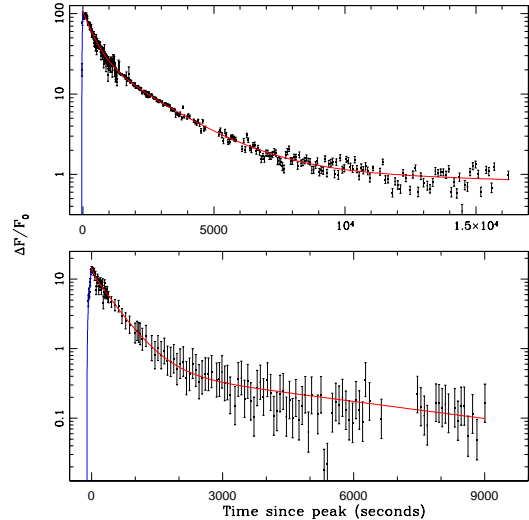


Figure 4. Light curves of the relative flare flux of GWAC 201221A (the upper panel) and GWAC 210117A (the lower panel). In each panel, the best fitted models in the rising phase and decaying phase are denoted by the blue and red lines, respectively.

Table 3. Best-fit parameters of the light curves of the two flares.

Parameter	Value	Parameter	Value
(1)	(2)	(3)	(4)
GWAC 201221A ($\chi^2/\text{dof} = 1.36$)			
a_0	1.060 ± 0.039	k_0	0.027 ± 0.002
a_1	0.00002 ± 0.00002	k_1	0.012 ± 0.002
a_2	0.00249 ± 0.00007	k_2	0.075 ± 0.013
a_3	$(5.1 \pm 0.2) \times 10^4$	k_3	0.307 ± 0.001
GWAC 210117A ($\chi^2/\text{dof} = 0.25$)			
a_0	0.6896 ± 0.04443	k_0	0.007 ± 0.001
a_1	0.0021 ± 0.0004	k_1	0.595 ± 0.065
a_2	0.0187 ± 0.0280	k_2	0.105 ± 0.082
a_3	0.0002 ± 0.0004	k_3	0.027 ± 0.040

5.2. Spectral analysis

In this section, we perform spectral analysis on the two flares by focusing on the profiles of the H α emission lines. The analysis enables us to identify a (redshifted) broad component that is potentially contributed by a flare-associated CME.

The signal-to-noise (S/N) ratio⁶ of the H α emission line in each spectrum is presented in the Column (4) of Table 2. With the S/N ratios and the profile decomposition described below, the minimum detectable CME mass $M_{\text{CME},\text{min}}$ could be estimated for the two events according to the Equation (9) in Odert et al. (2020), i.e.,

$$M_{\text{CME},\text{min}} \simeq \frac{\pi R_*^2 m_{\text{H}} N_{\text{H}}}{\text{SNR} \times W [1 - e^{-\tau}]} \quad (3)$$

where R_* is the radius of a host star, m_{H} the mass of hydrogen atom and N_{H} the column density of a prominence. W and τ are the geometric dilution factor and optical depth of H α emission line, respectively. By adopting the typical value of $W = 0.5$, N_{H} and $\tau = 10$ (Odert et al. 2020), $M_{\text{CME},\text{min}}$ is inferred to be 2.2×10^{16} g and 6.6×10^{16} g for GWAC 201221A and GWAC 210117A, respectively, when the basic properties of the host stars are adopted (see Table 5 in Section 6.1).

5.2.1. GWAC 201221A

In order to examining the variation of the H α line profile, a set of differential spectra are created by subtracting directly the last spectrum (i.e., No 11), which is guaranteed by the fixed object and sky apertures used in the extraction. The differential spectra of No. 1-10 are displayed in Figure 5. One can see from the figure that the No. 10 differential spectrum is dominated by random noise, which suggests a status close to the quiescent level for the last two spectra (i.e., No. 10 and 11, see also in Figure 2).

With the differential spectra, we then model the H α line profile by the SPECFIT task (Kriss 1994) in the IRAF package, which is shown in Figure 6, except the No. 10 spectrum. In each differential spectrum, the H α line profile is reproduced by a sum of a linear continuum and a set of Gaussian components. Two Gaussian components: one is narrow and another is broad (FWHM ~ 1000 km s⁻¹), are necessary for fitting the profile properly for the No. 1 to 6 spectra. However, the profiles in the next three spectra can be modeled properly by a single narrow Gaussian function.

The results of the line profile modeling are tabulated in Table 4. All the reported flux of the H α narrow component ($f(\text{H}\alpha_{\text{n}})$) includes the contribution from the

No. 11 spectrum of $f_0(\text{H}\alpha) = 7.9 \times 10^{-15}$ erg s⁻¹ cm⁻². Note that a correction of instrumental spectral resolution is ignored for all the reported widths of the narrow components. In contrast, a correction of $\sigma = \sqrt{\sigma_{\text{obs}}^2 - \sigma_{\text{inst}}^2}$ is applied for all the broad components, where σ_{inst} is the instrumental spectral resolution. The line shifts shown in Columns (6) and (7) are obtained from $\Delta v = c\Delta\lambda/\lambda_0$, where λ_0 and $\Delta\lambda$ are the rest-frame wavelength in vacuum of a given emission line and the wavelength shift of the line center, respectively. Column (8) lists the maximum projected velocity that is measured, from the observed spectrum, at the position where the H α high-velocity red wing merges to the continuum. Only the uncertainties, which are at the 1σ significance level, due to the modeling are reported in the table.

5.2.2. GWAC 210117A

In this flare, the relatively low S/N ratio of the continuum prevent us from building the differential spectra. We instead model the H α emission lines from the normalized spectra by a single Gaussian function. The results are tabulated in Table 4 as well.

Figure 7 compares the temporal evolution of the H α line profiles after a proper combination of the spectra taken at different epochs. The comparison clearly shows that there is a weak broad component in the first spectrum (the red curve). We then model the corresponding profile by a sum of two Gaussian functions as same as we did for GWAC 201221A to reproduce the red line wing. The best fit is shown in the inert panel in Figure 7, and presented in Table 4 as well. Again, a correction of the instrumental resolution is applied for the measured line width of the broad component.

6. RESULTS AND DISCUSSION

6.1. Quiescent Properties of the Two Stars

Based on their basic properties, we here argue that the host stars of both triggered events are M-dwarfs. With their G -band absolute magnitudes and $G_{\text{BP}} - G_{\text{RP}}$ colors, the two host stars are marked on the color-magnitude diagram (CMD) in Figure 8. One can see from the figure that 1) the host star of GWAC 210117A follows the main sequence of single stars very well; 2) the host star of GWAC 201221A locates slightly above GWAC 210117A. This elevation implies that the host star of GWAC 201221A is either a unresolved binary or a young main-sequence star (e.g., Gaia Collaboration et al. 2018b).

In addition, some basic parameters quoted from literature are tabulated in Table 5. The first row in the table shows the parameters of the host star of

⁶ In the estimate of S/N ratio of an emission line, the statistic error of the line σ_l is determined by the method given in Perez-Montero & Diaz (2003): $\sigma_l = \sigma_c \sqrt{N[1 + \text{EW}/(N\Delta)]}$, where σ_c is the standard deviation of continuum in a box near the line, N the number of pixels used to measure the line flux, EW the equivalent width of the line, and Δ the wavelength dispersion in units of \AA pixel⁻¹.

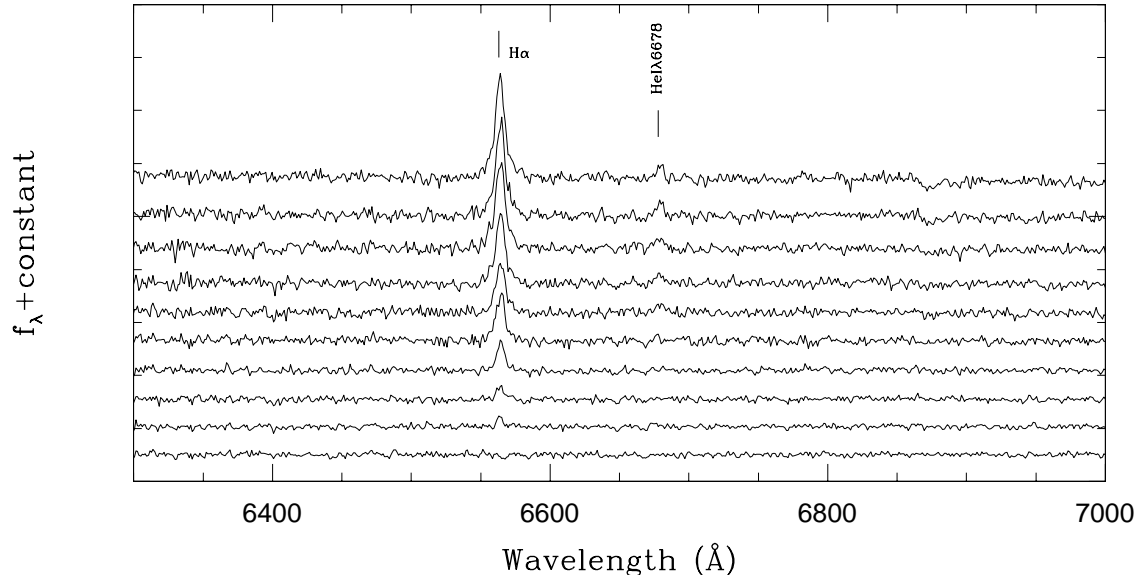


Figure 5. The same as in Figure 2 but for the differential spectra of GWAC 201221A.

GWAC 201221A determined from photometry by combining Gaia, Pan-STARRS1, 2MASS, and AllWISE by Anders et al. (2019). In the case, the spectral type of M4 is determined by the recently updated relationship between spectral type and T_{eff} (e.g., Pecaut & Mamajek 2013; Stassun et al. 2019). The parameters of the host star of GWAC 210117A are extracted from the updated stellar properties for the K2 stars in the Ecliptic Plane Input Catalog. The stellar properties, along with the spectral type of M4, are built by combining the Gaia distance and spectroscopy of the Large Sky Area Multi-Object Fiber Spectroscopic Telescope (LAMOST) DR5 (Hardegree-Ullman et al. 2019). However, a lower T_{eff} of $\sim 3000\text{--}3400\text{K}$, being more comparable with its spectral type of M4, can be found in other studies based on

photometry measurements (e.g., Boudreault et al. 2012; Ilin et al. 2019; Stassun et al. 2019; Cantat-Gaudin et al. 2020). In both events, the radius and mass of the host stars are extracted from Stassun et al. (2019).

6.2. Variation of $H\alpha$ Emission Lines

Based on the spectral analysis described in Section 5.2, the temporal evolution of the $H\alpha$ emission lines are shown in Figures 9 and 10 for GWAC 201221A and GWAC 210117A, respectively. As expected in a flare, the total $H\alpha$ line flux fades with time in both events. In GWAC 201221A, there is a significant variation of the broad $H\alpha$ component in flux, line width and maximum velocity, even though a lack of variation in the bulk velocity.

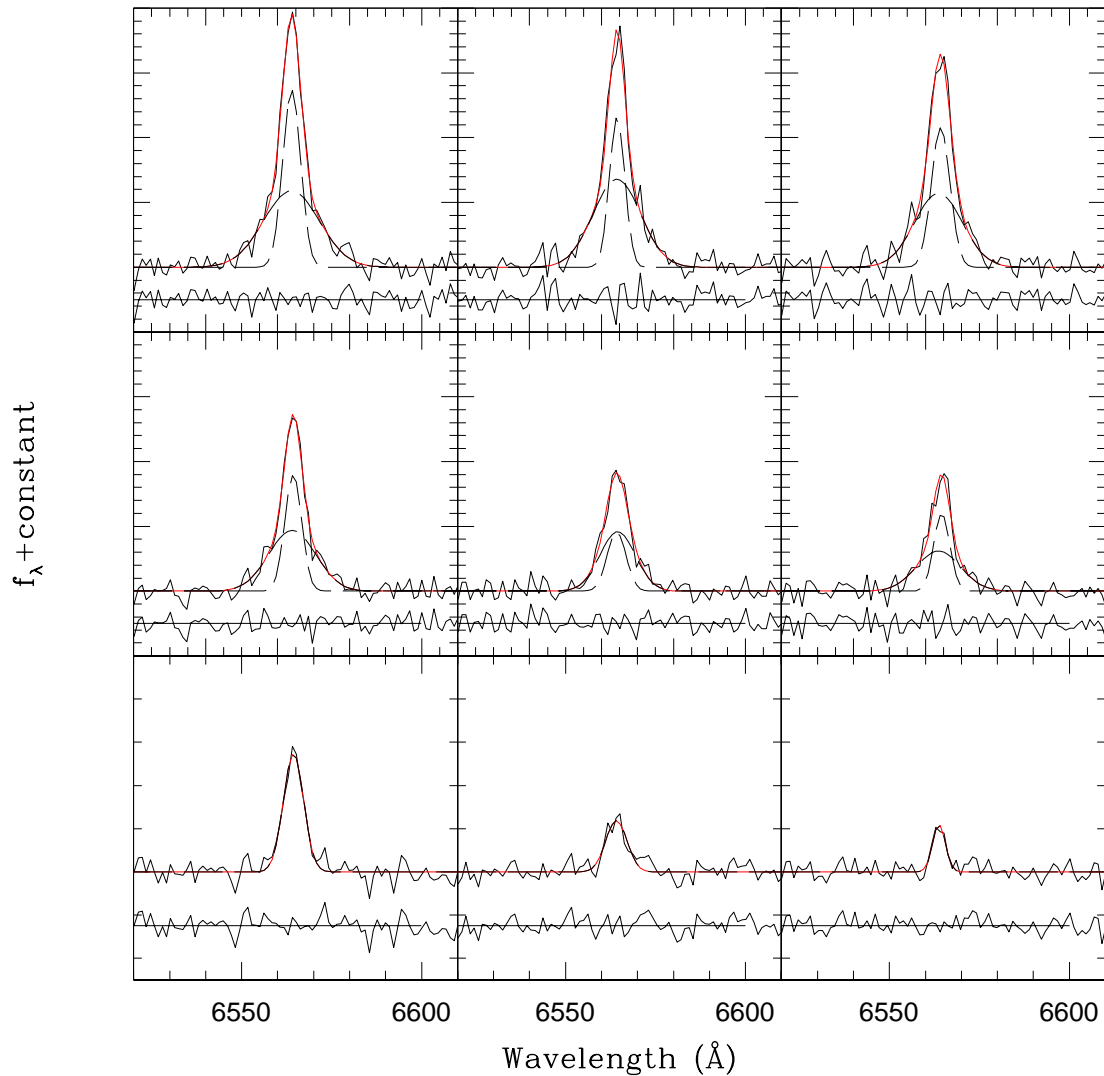


Figure 6. An illustration of line profile modelings by a linear combination of a set of Gaussian functions for the H α emission lines in GWAC 201221A. In each panel, the modeled local continuum has already been removed from the original observed spectrum. The observed and modeled line profiles are plotted by black and red solid lines, respectively. Each Gaussian function is shown by a dashed line. The sub-panel underneath the line spectrum presents the residuals between the observed and modeled profiles.

The measured large maximum velocities (V_{\max}) motivate us to argue that the detected broad H α emission is potentially resulted from the flare-associated CMEs in both events. At first, even though a blueshift signature leads to a more conclusive CME, both blueshift and redshift signatures could be observed as argued in Mouschou et al. (2019), both because of the projection effect and because of the random direction of an ejection (see Figure 4 in Mouschou et al. (2019)). Secondly, with the mass and radius listed in Table 5, the escape velocity $v_{\text{esc}} = 630(M/M_{\odot})^{1/2}(R/R_{\odot})^{-1/2}$ km s $^{-1}$ can be determined to be 620 km s $^{-1}$ and 610 km s $^{-1}$ at the

stellar surface for GWAC 201221A and GWAC 210117A, respectively. In GWAC 201221A, the determined v_{esc} is slightly smaller than the maximum of the measured V_{\max} . Although the measured V_{\max} is slightly smaller than the v_{esc} in GWAC 210117A, it is noted that the 1) the actual ejection velocity might be significantly larger than V_{\max} due to the projection effect (e.g., Houdebine et al. 1990), and 2) a smaller v_{esc} is expected if the plasma is ejected above the stellar surface (e.g., Lewis & Simmett 2002) because v_{esc} decrease with radius.

In addition to the CME scenario, the asymmetries of Balmer emission lines could be explained by chromo-

Table 4. Results of Spectral Measurements and Analysis.

ID	$f(\text{H}\alpha_n)$ ($10^{-15}\text{erg s}^{-1}\text{cm}^{-2}$)	$f(\text{H}\alpha_b)$ ($10^{-15}\text{erg s}^{-1}\text{cm}^{-2}$)	$\lambda_{\text{H}\alpha_n}$ (\AA)	$\lambda_{\text{H}\alpha_b}$ (\AA)	FWHM($\text{H}\alpha_n$)	FWHM($\text{H}\alpha_b$)	$\Delta v(\text{H}\alpha_n)$ (km s^{-1})	$\Delta v(\text{H}\alpha_b)$ (km s^{-1})	V_{max}
(1)	(2)	(3)	(4)	(5)	(6)	(7)	(8)	(9)	(10)
GWAC 201221A									
1	16.4 ± 1.1	11.5 ± 1.1	6563.9 ± 0.2	6563.8 ± 0.5	270 ± 20	770 ± 80	51 ± 9	47 ± 23	720
2	14.5 ± 1.2	11.3 ± 1.1	6564.3 ± 0.2	6564.2 ± 0.4	230 ± 20	630 ± 70	68 ± 9	64 ± 18	610
3	14.9 ± 1.1	9.5 ± 1.1	6564.3 ± 0.2	6563.6 ± 0.5	280 ± 20	630 ± 70	68 ± 9	37 ± 23	630
4	13.2 ± 0.8	7.7 ± 0.8	6564.4 ± 0.2	6564.1 ± 0.5	250 ± 20	620 ± 60	73 ± 9	59 ± 23	570
5	10.9 ± 2.0	5.7 ± 2.0	6564.2 ± 0.2	6564.5 ± 0.8	280 ± 70	410 ± 80	64 ± 27	78 ± 36	390
6	11.2 ± 2.2	4.7 ± 2.0	6564.5 ± 0.7	6563.6 ± 0.8	240 ± 70	570 ± 260	78 ± 32	37 ± 36	520
7	11.8 ± 0.2	6564.4 ± 0.2	300 ± 20	73 ± 9
8	9.7 ± 0.2	6564.1 ± 0.4	320 ± 40	59 ± 18
9	8.9 ± 0.2	6563.7 ± 0.4	190 ± 20	41 ± 18
GWAC 210117A									
1	28.2 ± 1.9	5.7 ± 1.1	6562.7 ± 0.3	6566.9 ± 1.9	400 ± 30	500 ± 110	-49 ± 13	210 ± 90	530
2	17.8 ± 1.2	6562.6 ± 0.2	360 ± 30	-54 ± 11
3	16.4 ± 1.2	6562.6 ± 0.3	340 ± 30	-56 ± 13
4	17.5 ± 1.1	6562.6 ± 0.2	370 ± 30	-56 ± 11
5	16.8 ± 0.6	6562.4 ± 0.1	360 ± 10	-64 ± 6
6	16.8 ± 0.7	6562.7 ± 0.1	360 ± 10	-51 ± 6
7	12.5 ± 0.4	6562.9 ± 0.1	320 ± 10	-42 ± 5

NOTE—Column (1): the number of spectrum in time series. Columns (2) and (3): the total flux in unit of $10^{-15}\text{erg s}^{-1}\text{cm}^{-2}$ of the $\text{H}\alpha$ narrow and broad component, respectively. Each component is denoted by a Gaussian function. Columns (4) and (5): the central wavelength unit of \AA of the $\text{H}\alpha$ narrow and broad component, respectively. Columns (6) and (7): the line width (full width at half maximum) unit of km s^{-1} of the $\text{H}\alpha$ narrow and broad component, respectively. Columns (8) and (9): the bulk velocity shift in unit of km s^{-1} with respect to the rest-frame wavelength of $\text{H}\alpha$ line. Column (10): the maximum velocity in unit of km s^{-1} of the broad $\text{H}\alpha$ line red wing (see the main text for the details).

Table 5. Basic parameters of the two host stars.

GWAC ID	Quiescent counterpart	T_{eff} (K)	$\log g$ (cm s^{-2})	Fe/H	Sp. Type	M_* (M_{\odot})	R_* (R_{\odot})	References
(1)	(2)	(3)	(4)	(5)	(6)	(7)	(8)	(9)
GWAC 201221A	SDSS J073908.7+171435.3	3213^{+10}_{-10}	$4.780^{+0.005}_{-0.007}$	$0.491^{+0.005}_{-0.186}$	M4	0.40 ± 0.03	0.41 ± 0.02	1,2
GWAC 210117A	EPIC 212002525	3694 ± 138	4.87 ± 0.06	0.114 ± 0.235	M4	0.32 ± 0.04	0.34 ± 0.01	2,3

NOTE—Column (1): the ID of the confirmed transient triggered by the GWAC system. Column (2): the name of the quiescent counterpart. Column (3): surface effective temperature in unit of K. Column (4): logarithmic of surface gravity in unit of cm s^{-2} . Column (5): Column (5): logarithmic of Fe to H abundance. Column (6): Spectral type. Columns (7) and (8): Mass and radius of the host star in unit of solar mass and solar radius, respectively. Column (9): the reference for the parameters: 1: Andres et al. (2019), 2: Stassun et al. (2019), 2: Hardegree-Ullman et al. (2020).

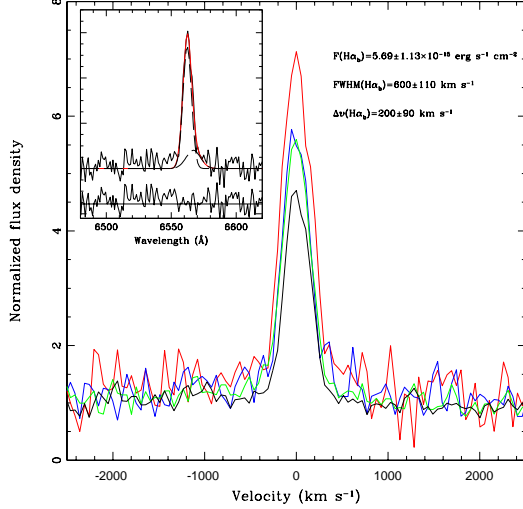


Figure 7. A comparison of the H α line profiles of GWAC 210117A, after a normalization with respect to the local continuum. The red and black curves correspond to the first (i.e., No. 1) and last (i.e., No. 7) spectra, respectively. The blue curve shows the profile after a combination of No. 2 and 3 spectra, and the green one the profile created from a combination of No. 4, 5 and 6 spectra. The insert panel shows the spectral modeling by a sum of two Gaussian profiles for the first spectrum. The symbols are the same as in Figure 6.

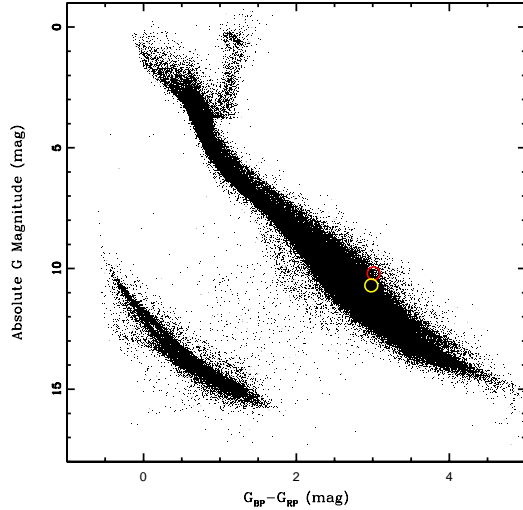


Figure 8. CMD of the Gaia stars. The stars at quiescent status are marked by the red and yellow circles for GWAC 201221A and GWAC 210117A, respectively.

spheric evaporation (Canfield et al. 1990; Gunn et al. 1994; Berdyugina et al. 1999), chromospheric condensation or coronal rain (e.g., Antolin et al. 2012; Lacatus et al. 2017; Vida et al. 2019; Fuhrmeister et al. 2018).

In the evaporation scenario, the chromospheric material can move either upward or downward due to the injected energy of the flare-accelerated electrons. On the Sun, the typical velocity of the chromospheric evaporation is about tens of km s^{-1} (Li et al. 2019) that is far below the V_{max} in GWAC 201221A, and far below both bulk velocity and V_{max} in GWAC 210117A. Although a chromospheric evaporation with $V_{\text{max}} \sim 600 \text{ km s}^{-1}$ was reported by Gunn et al. (1994) in a dMe4.5 star, the possibility of association with a CME is argued recently by Koller et al. (2021). The observations on the Sun indicate that the red asymmetry in H α emission line due to either chromospheric condensation or coronal rain shows velocity no more than $\sim 100 \text{ km s}^{-1}$ (e.g., Asai et al. 2012; Ichimoto & Kurokawa 1984), which is incompatible with the large bulk and (or) V_{max} observed in the current two flares.

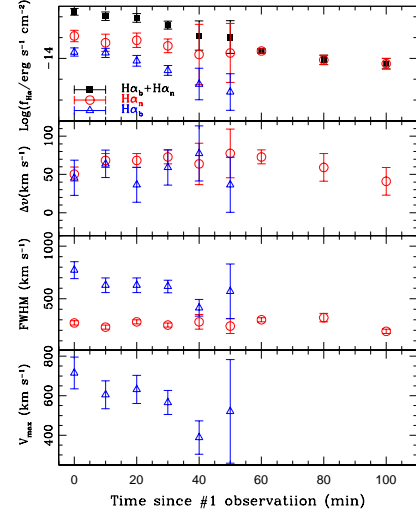


Figure 9. In GWAC 201221A, the temporal evolution of H α line flux, bulk velocity, line width and maximum projected velocity (V_{max}) during the flare are shown in the panels in an order from top to bottom.

6.3. CME Mass

The total line luminosity caused by a transition from level j to i is $L_{ji} = N_j A_{ji} h\nu_{ji} V P_{\text{esc}}$, where A_{ji} is the Einstein coefficient for a spontaneous decay from level j to i , N_j the number density of hydrogen atoms at excited level j , V the total volume and P_{esc} the escape probability. By considering $M_{\text{CME}} \geq N_{\text{tot}} V m_{\text{H}}$, the total hydrogen mass involved in a CME can then be estimated as (Koller et al. 2021; Houdebine et al. 1990):

$$M_{\text{CME}} \geq \frac{4\pi d^2 f_{\text{line}} m_{\text{H}} N_{\text{tot}}}{h\nu_{ji} A_{ji} P_{\text{esc}} N_j} \quad (4)$$

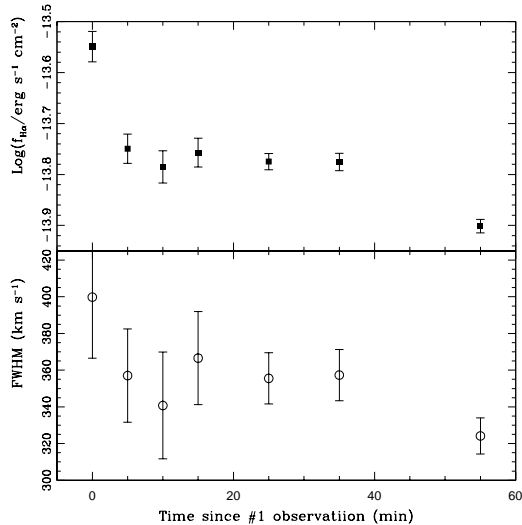


Figure 10. *Upper panel:* Temporal evolution of $H\alpha$ line flux for GWAC 210117A. *Lower panel:* The same as the upper one but for $H\alpha$ line width.

where d is the distance to the star, f_{line} the line flux due to a CME, m_{H} the mass of the hydrogen atom and N_{tot} is the number density of natural hydrogen atoms.

After transforming the observed $H\alpha$ line flux to $H\gamma$ by adopting a Balmer decrement of 3 (Butler et al. 1988), a mass of $1.5 - 4.5 \times 10^{19} \text{g}$ and $7.1 \times 10^{18} \text{g}$ can be obtained for GWAC 201221A and GWAC 210117A, respectively. In the calculations, we adopt $A_{52} = 2.53 \times 10^6$ (Wiese & Fuhr 2009) and $N_{\text{tot}}/N_5 = 2 \times 10^9$ estimated from non-local thermal equilibrium modeling (Houdebine & Doyle 1994a, b)⁷. We emphasize that only the modeled broad $H\alpha$ components are used in the mass estimations. A typical value of 0.5 is adopted for P_{esc} in the calculations (Leitzinger et al. 2014). We argue that the estimated masses are in fact in agreement with the previously expected range of 10^{14-19}g of a stellar CME (Moschou et al. 2019).

6.4. Flare energy

On the one hand, based on the method described in Kowalski et al. (2013), the total energy E_R in the R -band can be estimated from the formula: $E_R = 4\pi d^2 \times f_{R,q} \times ED$, where $f_{R,q}$ is the quiescent R -band flux determined previously in Section 2. With the distance and the determined ED, E_R is resulted to be $\sim 1.6 \times 10^{35} \text{erg}$ and $\sim 8.3 \times 10^{33} \text{erg}$ for GWAC 201221A and GWAC 210117A, respectively. The bolometric energy can then be estimated to be $E_{\text{bol}} \sim 9.6 \times 10^{35} \text{erg}$

⁷ We estimate the CME mass from the $H\gamma$ emission line, instead of $H\alpha$, because of a lack of N_3/N_{tot} in literature.

and $\sim 5.0 \times 10^{34} \text{erg}$ by adopting a bolometric correction of $L_{\text{bol}}/L_R = 6$. The bolometric correction is obtained by assuming a blackbody with an effective temperature of $T_{\text{eff}} = 10^4 \text{K}$.

On the other hand, it is known that there is a relationship between flare X-ray luminosity and $H\alpha$ luminosity given the statistical studies in both solar-like stars and more active stars (e.g., Bulter 1993; Martinez-Arnaiz et al. 2011). Based on the simple linear relationship of $L_X = 16L_{H\alpha}$ (i.e., Equation (1) in Mouschou et al. (2019)) and our spectroscopic and light curve analysis, the X-ray fluence of the flare is estimated to be $F_X = 5.3 \times 10^{34} \text{erg}$ and $2.1 \times 10^{34} \text{erg}$ for GWAC 201221A and GWAC 210117A, respectively.

The X-ray luminosity can be alternatively estimated from the $H\alpha$ emission according to the relationship, involving stellar surface flux, provided by Martinez-Arnaiz et al. (2011):

$$\log L_X = -2.72 + 1.48 \log L_{H\alpha} - 0.92 \log R_* \quad (5)$$

where R_* is the stellar radius. The relationship returns an X-ray fluence of $F_X = 8.4 \times 10^{34} \text{erg}$ and $2.7 \times 10^{34} \text{erg}$ for GWAC 201221A and GWAC 210117A, respectively, which are only slightly larger than the above values based on the simple linear relationship.

The ratio of white light to X-ray components in a stellar flare is now still poorly understood. With the above estimations, the ratio of F_X/E_{bol} is $\approx 0.05 - 0.08$ in GWAC 201221A, which roughly agrees with the result of ≈ 0.01 revealed by the solar observations (e.g., Kretzschmar 2011; Emslie et al. 2012). A much larger $F_X/E_{\text{bol}} \approx 0.4 - 0.5$ is, however, obtained for GWAC 210117A, which could be explained by the fact that Martinez-Arnaiz et al. (2011) suggests that there is an equipartition between X-ray and Balmer line emission for the flares with low fluence.

7. CONCLUSION

Thanks to the high cadence survey of the GWAC system, fast and time-resolved spectroscopic follow-ups are carried out for two M-dwarf flares. The light curve analysis indicates a flare energy in R -band of $1.6 \times 10^{35} \text{erg}$ and $8.1 \times 10^{33} \text{erg}$. High velocity wings of their $H\alpha$ emission lines can be identified in both flares. The large projected maximum velocity of $\sim 500 - 700 \text{km s}^{-1}$ motivates us to argue that the wings are most likely resulted from a CME event, after excluding the possibility of chromospheric evaporation and coronal rain. With the modeling of the $H\alpha$ emission line profiles, the CME masses are estimated to be $1.5 - 4.5 \times 10^{19} \text{g}$ and $7.1 \times 10^{18} \text{g}$.

ACKNOWLEDGMENTS

The authors thank the anonymous referee for a careful review and helpful suggestions that improved the manuscript greatly. The authors are thankful for support from the National Key R&D Program of China (grant No. 2020YFE0202100). The study is supported by the National Natural Science Foundation of China under grants 11773036 and U1821207, and by the Strategic Pioneer Program on Space Science, Chinese Academy of Sciences, grants No. XDA15052600 and XDA15016500. J.W. is supported by the Natural Science Foundation of Guangxi (2020GXNSFDA238018), and by the Bagui Young Scholars Program. We thank the night assistants and duty astronomers of the NAOC 2.16m telescope and the GWAC system for their instrumental and ob-

servational help. This work has made use of data from the European Space Agency (ESA) mission Gaia (<https://www.cosmos.esa.int/gaia>), processed by the Gaia Data Processing and Analysis Consortium (DPAC, <https://www.cosmos.esa.int/web/gaia/dpac/consortium>). Funding for the DPAC has been provided by national institutions, in particular the institutions participating in the Gaia Multilateral Agreement. This research has made use of the Vizier catalog access tool, CDS, Strasbourg, France (doi: 10.26093/cds/vizier). The original description of the Vizier service was published in A&AS 143, 23.

Facilities: GWAC, GWAC-F60A, NAOC 2.16m telescope

Software: IRAF (Tody 1986, 1992), Python

REFERENCES

- Aarnio, A. N., Stassun, K. G., Hughes, W. J., & McGregor, S. L. 2011, *SoPh*, 268, 195
- Ambruster, C. W., Pettersen, B. R., & Sundland, S. R. 1989, *A&A*, 208, 198
- Anders, F., Khalatyan, A., Chiappini, C., Queiroz, A. B., Santiago, B. X., Jordi, C., Girardi, L., Brown, A. G. A., et al. 2019, *A&A*, 628, 94
- Antolin, P., Vissers, G., & Rouppe van der Voort, L. 2012, *SoPh*, 280, 457
- Argiroffi, C., Reale, F., Drake, J. J., et al. 2019, *Nature Astronomy*, 3, 742
- Asai, A., Ichimoto, K., Kita, R., Kurokawa, H., & Shibata, K. 2019, *PASJ*, 64, 20
- Balona, L. A. 2015, *MNRAS*, 447, 2714
- Berdugina, S. V., Ilyin, I., & Tuominen, I. 1999, *A&A*, 349, 863
- Boudreault, S., Lodieu, N., Deacon, N. R., & Hambly, N. C. 2012, *MNRAS*, 426, 3419
- Butler, C. J. 1993, *A&A*, 272, 507
- Butler, C. J., Rodono, M., & Foing, B. H. 1988, *A&A*, 206, L1
- Cantat-Gaudin, T., Anders, F., Castro-Ginard, A., Jordi, C., Romero-Gomez, M., Soubiran, C., Casamiquela, L., Tarricq, Y., et al. 2020, *A&A*, 640, 1
- Canfield, R. C., Penn, M. J., Wulser, J., & Kiplinger, A. L. 1990, *ApJ*, 363, 318
- Chandra, R., Chen, P. F., Fulara, A., Srivastava, A. K., & Uddin, W. 2016, *ApJ*, 822, 106
- Chang, H. -Y., Lin, C. -L., Ip, W. -H., Huang, L. -C., Hou, W. -C., Yu, P. -C., Song, Y. -H., & Luo, A. 2018, *ApJ*, 867, 78
- Cherenkov, A., Bisikalo, D., Fossati, L., & Mostl, C. 2017, *ApJ*, 846, 31
- Davenport, J. R. A., Hawley, S. L., Hebb, L., et al. 2014, *ApJ*, 797, 122
- Davenport, J. R. A., Kipping, D. M., Sasselov, D., Matthews, J. M., & Cameron, C. 2016, *ApJL*, 829, 31
- Emslie, A. G., Dennis, B. R., Shih, A. Y., et al. 2012, *ApJ*, 759, 71
- Fan, Z., Wang, H. J., Jiang, X. J., et al. 2016, *PASP*, 128, 5005
- Forbes, T. G., Linker, J. A., Chen, J., et al. 2006, *SSR*, v, 123, 251
- Fuhrmeister, B., Czesla, S., Schmitt, J. H. M. M., et al. 2018, *A&A*, 615, 14
- Gaia Collaboration, Brown, A. G. A., Vallenari, A., et al. 2018a, *A&A*, 616, 1
- Gaia Collaboration, Brown, A. G. A., Vallenari, A., et al. 2018b, *A&A*, 616, 10
- Gunn, A. G., Doyle, J. G., Mathioudakis, M., Houdebine, E. R., & Avgoloupis, S. 1994, *A&A*, 285, 489
- Hardegree-Ullman, K. K., Zink, J. K., Christiansen, J. L., Dressing, C. D., Ciardi, D. R., & Schlieder, J. E. 2020, *ApJS*, 247, 28
- Houdebine, E. R., & Doyle, J. G. 1994a, *A&A*, 289, 169
- Houdebine, E. R., & Doyle, J. G. 1994b, *A&A*, 289, 185
- Houdebine, E. R., Foing, B. H., & Rodono, M. 1990, *A&A*, 238, 249

- Huenemoerder, D. P., Schulz, N. S., Testa, P., Drake, J. J., Osten, R. A., & Reale, F. 2010, *ApJ*, 723, 1558
- Ichimoto, K., & Kurokawa, H. 1984, *SoPh*, 93, 105
- Ilin, E., Schmidt, S. J., Davenport, J. R. A., & Strassmeier, K. G. 2019, *A&A*, 622, 133
- Karlicky, M., & Barta, M. 2007, *A&A*, 464, 735
- Kliem, B., Karlicky, M., & Benz, A. O. 2000, *A&A*, 360, 715
- Koller, F., Leitzinger, M., Temmer, M., Odert, P., Beck, P. G., & Veronig, A. 2021, *A&A*, 646, 34
- Kowalski, A. F., Hawley, S. L., Wisniewski, J. P., Osten, R. A., Hilton, E. J., Holtzman, J. A., Schmidt, S. J., Davenport, J. R. A. 2013, *ApJS*, 207, 15
- Kretzschmar, M. 2011, *A&A*, 530, 84
- Kriss, G. 1994, in *ASP Conf. Ser. 61, Astronomical Data Analysis Software and Systems III*, ed. D. R. Crabtree, R. J. Hanisch, & J. Barnes (San Francisco, CA: ASP), 437
- Lacatus, D. A., Judge, P. G., Donea, A., Daniela A., Judge, P. G., & Donea, A. 2012, *ApJL*, 842, 15
- Leitzinger, M., Odert, P., Greimei, R., Korhonen, H., Guenther, E. W., Hanslmeier, A., Lammer, H., & Khodachenko, M. L. 2014, *MNRAS*, 443, L898
- Li, Y., Ding, M. D., Hong, J., Li, H., & Gan, W. Q. 2019, *ApJ*, 879, 30
- Li, L., Zhang, J., Peter, H., et al. 2016, *Nature Physics*, 12, 847
- Martinez-Arnaiz, R., Lopez-Santiago, J., Crespo-Chacon, I., & Montes, D. 2011, *MNRAS*, 414, 2629
- Massey, P., Strobel, K., Barnes, J. V., et al. 1988, *ApJ*, 328, 315
- Moschou, S., Drake, J. J., Cohen, O., Alvarado-Gomez, J. D., & Garraffo, C. 2017, *ApJ*, 850, 191
- Moschou, S., Drake, J. J., Cohen, O., Alvarado-Gomez, J. D., Garraffo, C., & Frascchetti, F. 2019, *ApJ*, 877, 105
- Notsu, Y., Maehara, H., Shibayama, T., Honda, S., Notsu, S., Namekata, K., Nogami, D., & Shibata, K. 2016, *The 19th Cambridge Workshop on Cool Stars, Stellar Systems, and the Sun (CS19)*, Uppsala, Sweden, 06-10 June 2016, id.119
- Noyes, R. W., Hartmann, L. W., Baliunas, S. L., Duncan, D. K., & Vaughan, A. H. 1984, *ApJ*, 279, 763
- Odert, P., Leitzinger, M., Guenther, E. W., & Heinzl, P. 2020, *MNRAS*, 494, 3766
- Osten, R. A., Brown, A., Ayres, T. R., et al. 2004, *ApJS*, 153, 317
- Osten, R. A., Hawley, S. L., Allred, J. C., Johns-Krull, C. M., & Roark, C. 2005, *ApJ*, 621, 398
- Paudel, R. R., Gizis, J. E., Mullan, D. J., Schmidt, S. J., Burgasser, A. J., Williams, P. K. G., & Berger, E. 2018, *ApJ*, 858, 55
- Pecaut, M. J., & Mamajek, E. E. 2013, *ApJS*, 208, 9
- Pettersen, B. R. 1989, *A&A*, 209, 279
- Perez-Montero, E., & Diaz, A. I. 2013, *MNRAS*, 346, 105
- Schlafly, E. F., & Finkbeiner, D. P. 2011, *ApJ*, 737, 103
- Schmidt, S. J., Shappee, B. J., van Saders, J. L., et al. 2019, *ApJ*, 876, 115
- Schmitt, J. H. M. M. 1994, *ApJS*, 90, 735
- Shulyak, D., Reiners, A., Engeln, A., Malo, L., Yadav, R., Morin, J., & Kochukhov, O. 2017, *Nature Astronomy*, 1, 184
- Stassun, K. G., Oelkers, R. J., Paegert, M., Torres, G., Pepper, J., De Lee, N., Collins, K., Latham, D. W., et al., 2019, *AJ*, 158, 138
- Tody, D. 1986, *Proc. SPIE*, 627, 733
- Tody, D. 1993, in *ASP Conf. Ser. 52, Astronomical Data Analysis Software and Systems II*, ed. R. J. Hanisch, R. J. V. Brissenden, & J. Barnes (San Francisco, CA: ASP), 173
- Tsuneta, S. 1996, *ApJ*, 456, 840
- Van Doorselaere, T., Shariati, H., & Debosscher, J. 2017, *ApJS*, 232, 26
- Vida, K., Leitzinger, M., Kriskovics, L., Seli, B., Odert, P., Kovacs, O., Korhonen, H., van Driel-Gesztelyi, L. 2019, *A&A*, 623, 49
- Wang, J., Li, H. L., Xin, L. P., et al. 2020, *AJ*, 159, 35
- Wei, J. Y., Cordier, B., Antier, S., et al. 2016, arXiv:1610.0689
- Webb, D. F., & Howard, T. A. 2012, *LRSP*, 9, 3
- Wiese, W. L., & Fuhr, J. R. 2009, *JPCRD*, 38, 565
- Wright, N. J., Drake, J. J., Mamajek, E. E., & Henry, G. W. 2011, *ApJ*, 743, 48
- Xin, L. P., Li, H. L., Wang, J., et al. 2021, *ApJ*, 909, 106
- Xu, Y., Xin, L. P., Wang, J., Han, X. H., Qiu, Y. L., Huang, M. H., & Wei, J. Y. 2020, *PASP*, 132, 054502
- Yashiro, S., Michalek, G., Akiyama, S., Gopalswamy, N., & Howard, R. A. 2008, *ApJ*, 673, 1174